A Bioinspired and Scalable Near-ideal Broadband Coating for Radiative Thermoregulation.

Xihao Song, Yongfeng Gao, and Peng Zhang*

This Supporting Information contains:

Supplemental Notes: Note S1-S3

Supplemental Figure: Fig. S1-S18

Supplemental Video: Video S1

Supplemental References: 1-8

Supplemental Note 1 Defination of the averaged optical parameters

The averaged solar reflectance ($\overline{R}_{solar}$) and the averaged emissivity over the main atmospheric window ($\overline{\varepsilon}_{8\text{-}13\,\mu m}$) are defined as:

$$\overline{R}_{solar} = \frac{\int_{0.3\,\mu m}^{2.5\,\mu m} I_{solar}(\lambda)\cdot R(\lambda)d\lambda}{\int_{0.3\,\mu m}^{2.5\,\mu m} I_{solar}(\lambda)d\lambda} \tag{S1}$$

$$\overline{\varepsilon}_{8-13\,\mu m} = \frac{\int_{8\,\mu m}^{13\,\mu m} \varepsilon(\lambda)\cdot I_{black}(\lambda,T)d\lambda}{\int_{8\,\mu m}^{13\,\mu m} I_{black}(\lambda,T)d\lambda} \tag{S2}$$

where λ is the wavelength, $I_{solar}(\lambda)$ is the AM 1.5 global solar intensity spectrum and $R(\lambda)$ represents the spectral reflectance of the coating. In addition, $I_{black}(\lambda, T)$ is the spectral blackbody radiant intensity defined by the Planck's law and $\varepsilon(\lambda)$ indicates the spectral emissivity of the coating. For the ease of illustration, the reflectance over 2.5-8 μm is also averagely weighted by the blackbody thermal irradiance[1]:

$$\overline{R}_{2.5-8\,\mu m} = \frac{\int_{2.5\,\mu m}^{8\,\mu m} I_{black}(\lambda)\cdot R(\lambda)d\lambda}{\int_{2.5\,\mu m}^{8\,\mu m} I_{black}(\lambda)d\lambda} \tag{S3}$$

Supplemental Note 2 Principles of cooling power estimation of the daytime radiative cooling

When the passive daytime radiative cooling (PDRC) coating is placed under the clear sky in daytime, it emits thermal energy and simultaneously is heated by the irradiation from the sun and the atmosphere and the parasitic heat of the conduction and convection. The net cooling power of the PDRC coating $P_{net}(T)$ can be formulated with the ambient temperature T_a and the temperature of the radiative cooling coating T,

$$P_{\text{net}}(T) = P_{\text{rad}}(T) - P_{\text{sun}} - P_{atm}(T_a) - P_{conv+cond}(T, T_a) \tag{S4}$$

where, $P_{rad}(T)$ indicates the outward emission power of the PDRC coating, $P_{sun}(T)$ indicates the solar irradiation power absorbed by the coating, $P_{atm}(T_a)$ refers to the absorbed atmospheric irradiation power, and $P_{conv+cond}(T)$ is the the parasitic heat due to convective and conductive heat transfer. $P_{rad}(T)$ can be estimated by the following formula:

$$P_{\text{rad}}(T) = \int_0^{2\pi} \int_0^{\infty} \varepsilon(\lambda, \theta) \cos\theta I_B(T, \lambda) \mathrm{d}\lambda \mathrm{d}\Omega \tag{S5}$$

where, ε (λ, θ) refers to the spectral-angular emissivity of the radiative coating. λ and θ represent the wavelength and zenith angle, respectively. $I_B(T, \lambda)$ is the spectral radiation intensity of black body at the temperature of T, formulated as:

$$I_B(T, \lambda) = \frac{2hc_0^2}{\lambda^5} \frac{1}{\exp(hc_0 / \lambda k_B T) - 1} \tag{S6}$$

where, h is the Planck constant, c_0 is the speed of light and k_B is the Boltzmann constant. The absorbed solar and atmospheric thermal radiation of the PDRC coating can be formulated as:

$$P_{\text{sun}} = \int_0^{\infty} \varepsilon(\lambda, \theta) I_{AM1.5}(\lambda) \mathrm{d}\lambda \tag{S7}$$

$$P_{\text{atm}}(T_a) = \int_0^{2\pi} \int_0^{\infty} \varepsilon_{atm}(\lambda, \theta) \varepsilon(\lambda, \theta) \cos\theta I_B(T_a, \lambda) \mathrm{d}\lambda \mathrm{d}\Omega \tag{S8}$$

where, the $I_{AM1.5}(\lambda, \theta)$ is the AM 1.5 spectrum of the solar irradiation and $\varepsilon_{\text{atm}}(\lambda, \theta)$ is the directional emissivity of atmosphere, which can be expressed in term of the

transmissivity of the atmosphere in the vertical direction $\tau(\lambda, \theta)$, namely $\varepsilon_{atm}(\lambda,\theta) = 1-\tau(\lambda)^{1/\cos\theta}$. Moreover, the heat loss by convective and conductive heat transfer is defined as:

$$P_{conv+cond}(T, T_a) = h_c\left(T - T_a\right) \tag{S9}$$

where, h_c is heat transfer coefficient including both the convective and conductive heat transfer.

For the results shown in Fig. S1 and Fig. S9, i.e., the theoretical net cooling powers of six different representative radiative cooling coatings, including the ideal selective coating, ideal broadband coating, the dual-layer coating, the porous monolayer coating, and coatings in Ref. S2 and Ref. S3, were conducted based on the aforementioned Eqs. S4-S9, where the spectral reflectance data (ρ) of the dual-layer coating and the porous monolayer coating are from Fig. 2b and the spectral reflectance data of other four radiative cooling coatings, namely the ideal broadband coating, ideal selective coating and the PDRC coatings in Ref. S2 and Ref. S3, are illustrated in Fig. S9c. The corresponding spectral emissivity (ε) can be derived by ε=1-ρ. The ambient temperature was set as 300 K and the h_c was set as zero to eliminate the effect of the heat loss by convective and conductive heat transfer. In addition, the AM 1.5 and US standard 1976 model were applied for the characterization of the solar irradiance and the atmospheric transmittance, respectively.

For the results shown in Fig. S18c, the maximum temperature drops of five dual-layer coating specimens, namely white, orange, red, blue and green, versus the incident solar irradiance were estimated by Eq. S4. The $P_{rad}(T)$, $P_{atm}(T_a)$ and $P_{conv+cond}(T, T_a)$ still follow the definition in Eqs. S5, S8 and S9, respectively, while the absorbed solar irradiance was evaluated based on Eq. S10, defined as:

$$P_{\text{sun}} = (1-\bar{R}_{solar}) \times E_{solar} \tag{S10}$$

where the E_{solar} represents the total solar irradiance. The relevant spectral reflectance data can be derived from Fig. 6e and Fig. S18b. In this manner, the maximum temperature drop of a specific specimen at a certain solar irradiance can be obtained

as the net cooling power is zero. In addition, the ambient temperature was also set as 300 K and the h_c was set as zero. The atmospheric transmittance is still characterized by US standard 1976 model.

Supplemental Note 3 The simulation of optical properties

The reflectance of the dual-layer coating was theoratically simulated through the DiffractMOD module of commercial software Rsoft using the rigorous coupled-wave theory (RCWA) method to achieve an accurate solution of the Maxwell equation based on the given complex refractive index of the materials and the composite structure of the coating.[4] Since it has been proved that the 2D simulation is able to approcimaterly reflect the result of 3D simulation,[5] to reduce the computational load, the 2D dual-layer coating model, including a dense layer and a nano/micro porous layer, was constructed by the built-in CAD system in Fig. S10. The nano and micro voids within the porous layer were built based on the statistic results of the pore size distribution in Fig. 2c. To simplify simulation, the pore sizes of both nanopores and micropores were selected to represent the total pore size distribution, where the diameters of 200, 300, 500 and 1000 nm were for nanopores and the diameters of 2, 3, 4 and 5 μm were for micropores (Fig. S10). Besides, the total volume ratio of nanopores and micropores was set as 1: 1 and the overall porosity of the porous layer was around 50%. The periodical boundary conditions were applied at the left and right boundaries of model. Then, the interior electromagnetic field was simulated and the reflectance can be obtained from the postprocess of the known electromagnetic field.

For the simulation in Fig. 3a, Fig. 3b-I and Fig. S11a, since the absorbance feature of the poly(vinylidene fluoride) (PVDF) is similar to that of the poly(vinylidene fluoride-co-hexafluoropropene) (PVDF-HFP) (Fig. S6), the complex refractive index used in the simulation was that of the PVDF-HFP for simplication. For the simulation model in Fig. 3a, the thickness of the dense layer was set as 200 μm and the thickness of the porous layer was chosen as 360 μm. To evidence that the

proposed dual-layer structure can also achieve the near-ideal broadband emission in other PDRC polymers (Fig. S12), the polymethyl methacrylate (PMMA) and polydimethylsiloxane (PDMS) were selected and applied in the aforementioned model (Fig. S10) where the thicknesses of the dense layer and porous layer were 200 μm and 360 μm, respectively. The simulated spectral reflectance reveals that the near-ideal broadband emission can be attained through the proposed dual-layer structure (Fig. S12). To predict the spectral reflectance at varying thicknesses of the dense layer, similar simulations were conducted by varying the thickness of the concerned layer, as shown in Fig. 3b-I and Fig. S11a. For example, to investigate the effect of thickness of the dense layer on the reflectance, the thickness of the dense layer was set as 0, 30, 50, 100 and 200 μm, respectively and other conditions, like the complex refractive index of the PVDF-HFP and air, the thickness of the porous layer and the boundary conditions, were kept unchanged.

Supplemental Figures

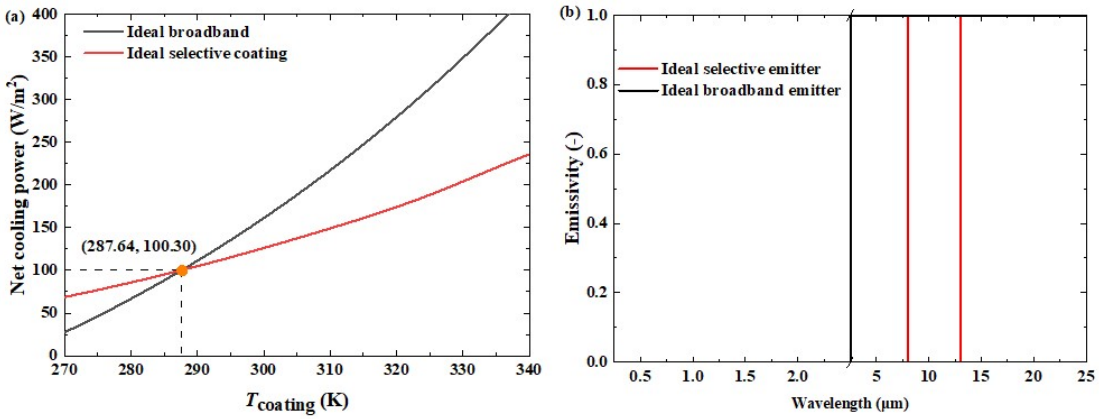

Fig. S1. Comparison between the ideal broadband coating and the ideal selective coating. (a) Comparison of the net cooling powers between the ideal broadband coating and ideal selective coating at varying temperatures of the coating ($T_{coating}$). Above the cross point, the net cooling power of the ideal broadband coating is larger than that of the ideal selective coating. (b) The spectral emissivity of the ideal broadband coating and ideal selective coating, respectively.

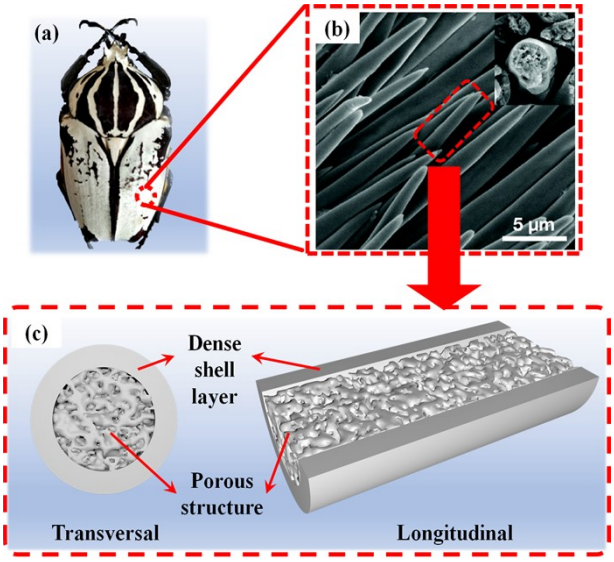

Fig. S2. Morphology and schematic illustration of the scales of the white beetle *Goliathus goliatus*. (a) Photograph of a specimen of the white beetle *Goliathus goliatus*.[6] (b) Scanning electron microscopy (SEM) image of the scales on the exocuticle of the elytra. The inset depicts the cross-sections of the dense scales.[7] (c) The transversal and longitudinal sectional sketches of a single scale. It has been proved by Xie et al.[7] that significant solar reflectance of the scale is attributed to the synergetic effect of thin-film interference and Mie resonance, led by the exterior dense layer and the interior porous structure, respectively. In addition, the elytra with scales exhibits higher emissivity in the wavelength range of 4-14 μm compared with the bare elytra without scales. On the one hand, the composition of the scale is chitin, which strongly absorbs/emits in the 8-13 μm due to the vibration of the chemical bonds. On the other hand, the shell-pore structure leads to a continuous refractive index gradient between the medium and air so that the reflectance in the infrared wavelength range can be effectively decreased.

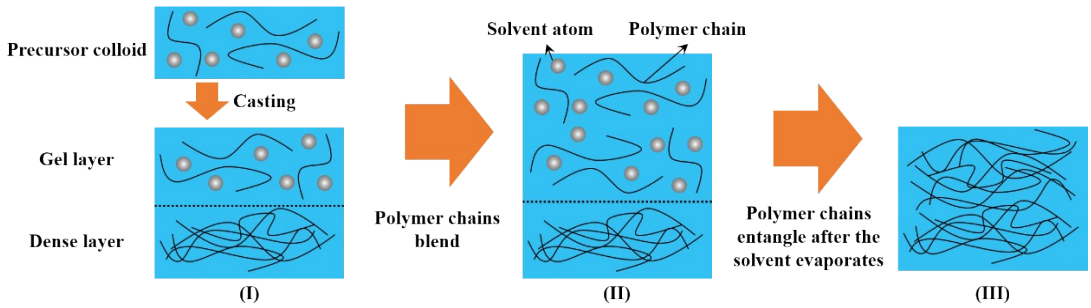

Fig. S3. The schematic illustration of the entanglement process of the polymer chains from the dense layer and the precursor colloid, which leads to a strong bond between the porous and dense layers of the dual-layer coating. Before the acetone-swelled dense layer completely dries, there is

a thin gel layer containing both solvent (acetone) and PVDF chains on the surface of the dense layer (I), which allows the PVDF-HFP chains from the casted precursor colloid to penetrate and interconnect with PVDF chains (II). After the solvent evaporates, the polymer chains entangle together to strongly interconnect the dense layer and porous layer (III).

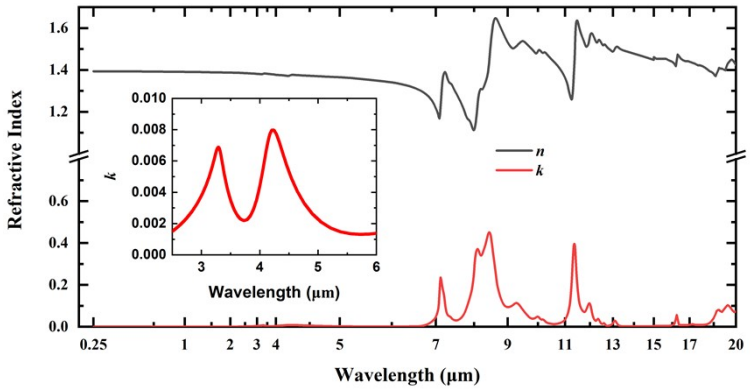

Fig. S4. The spectral complex refractive index of the PVDF-HFP from 0.25 to 20 μm.[8]

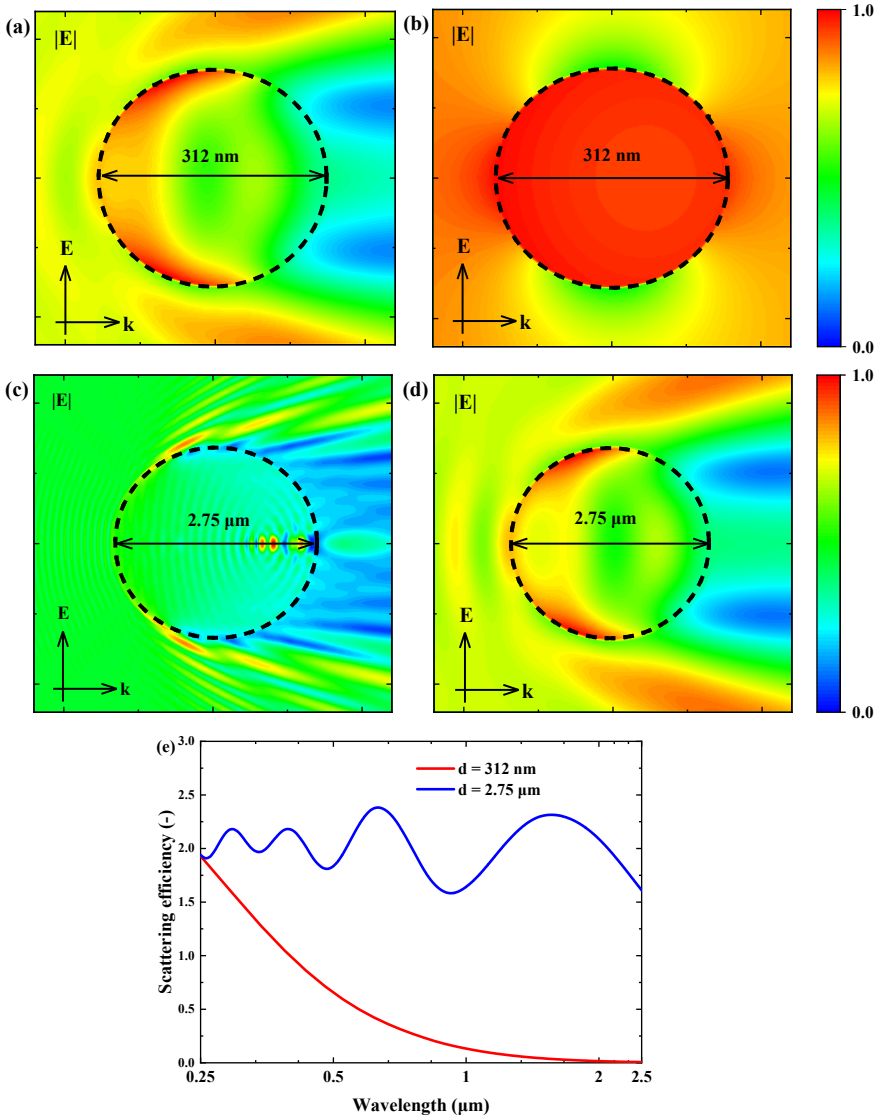

Fig. S5. Theoretical simulation of the electric field and scattering efficiency of the air void embodied in PVDF-HFP substrate. (a and b) The electric field distribution of the air void embodied in PVDF-HFP substrate with the diameter of d = 312 nm. The wavelengths of the incident light sources are 0.25 μm (a) and 2.0 μm (b), respectively. It is observed that the air void with the diameter of d = 312 nm shows significant back-scattering at the wavelength of 0.25 μm while the scattering is slight at the wavelength of 2.0 μm. (c and d) The electric field distribution of the air void embodied in PVDF-HFP substrate with the diameter of d = 2.75 μm. Pronounced back-scattering effect is found at both the wavelengths of 0.25 μm and 2.0 μm. The wavelengths of the incident light sources are 0.25 μm (c) and 2.0 μm (d), respectively. The results in the insets of Fig. 2c and Fig. S5a-d were obtained by applying the Fullwave module in Rsoft. (e) The scattering efficiency of the air voids with the diameters of d= 312 nm and 2.75 μm in PVDF-HFP

substrate in the wavelength range of 0.25-2.5 μm, respectively. This simulation was conducted based on the Lorenz-Mie scattering theory [9] and the results reveal that the air voids with the diameters of *d*= 312 nm and 2.75 μm in PVDF-HFP substrate can effectively scatter the solar irradiance, where the air voids with the diameter of *d*= 2.75 μm show better efficiency at larger wavelength.

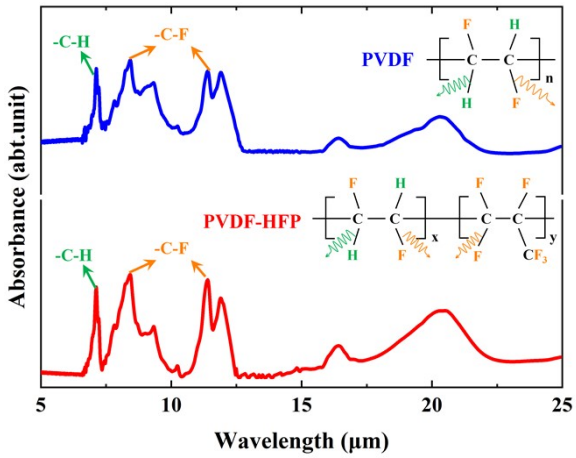

Fig. S6. The absorbance spectrum of the PVDF and PVDF-HFP, which was characterized by the Fourier-transform-based infrared spectrometer (Nicolet 6700, Thermo Fisher Scientific). Moreover, since the PVDF owns similar feature of molecular bonds vibration to that of PVDF-HFP, it can be deduced that the PVDF exbibits similar absorption characteristics to PVDF-HFP so that the complex refractive index of PVDF is considered as similar to that of the PVDF-HFP.

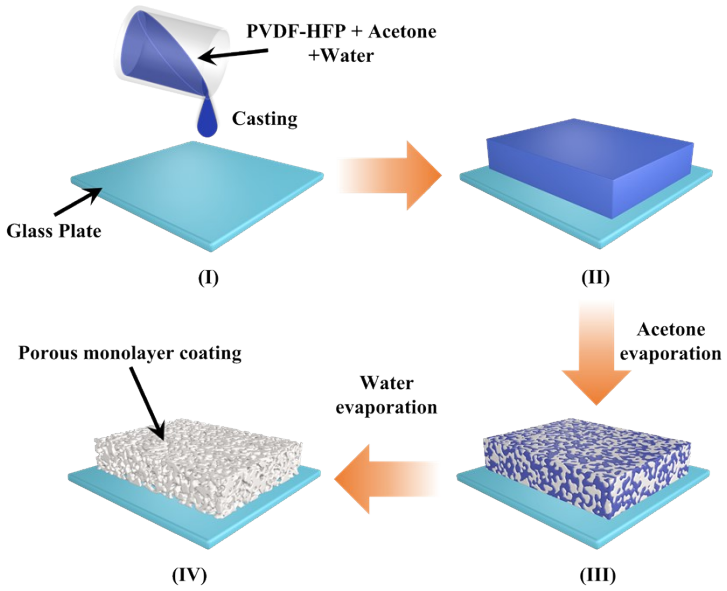

Fig. S7. The schematic illustration of the fabrication process of the porous monolayer coating.

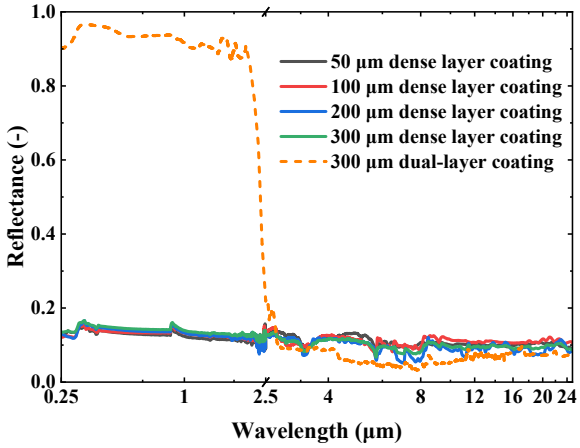

Fig. S8. The spectral reflectance of the pure dense layer coating at varying thicknesses. The reflectance of the 300 μm-thick dual-layer coating composed of 50 μm-thick dense layer and 250. μm-thick porous layer is also presented for comparison. It can be seen that the reflectance of the dense layer coating with varying thicknesses fluctuates around ~0.11 over the entire wavelength range of 0.25-25 μm.

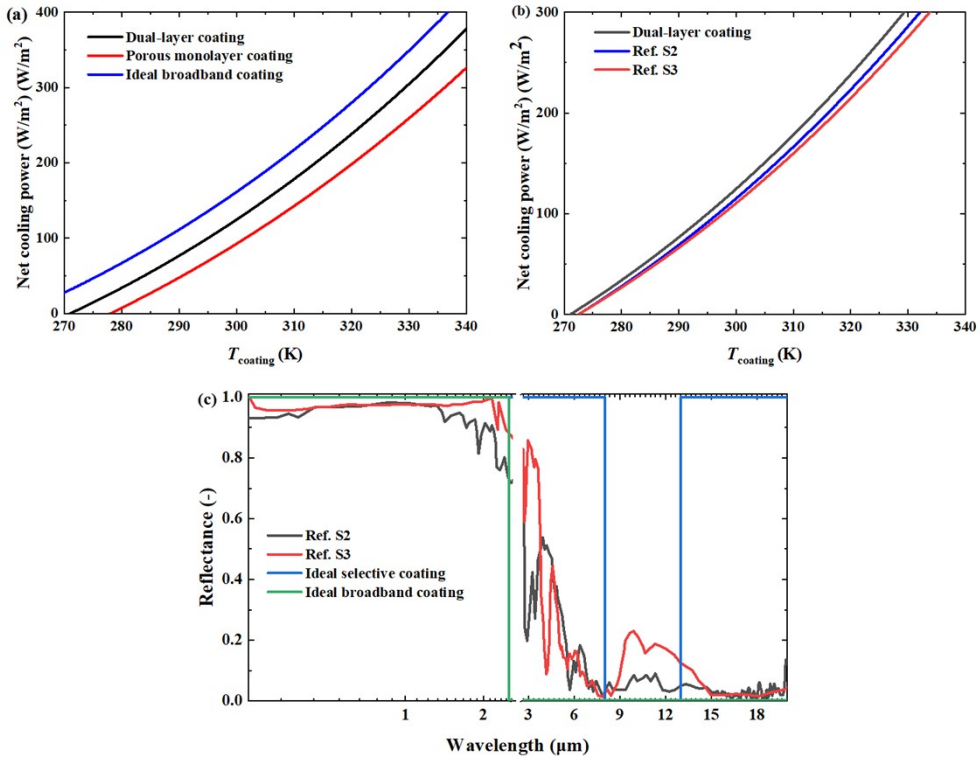

Fig. S9. Comparison of the theoretical net cooling power among different radiative cooling coatings. (a) Comparison of the theoretical net cooling powers of the dual-layer coating, the porous monolayer coating and the ideal broadband coating at varying temperatures of the coating ($T_{coating}$), where the net cooling power of the dual-layer coating surpasses that of the porous

monolayer coating and the dual-layer coating achieves a lower temperature compared with the porous monolayer coating when the net cooling power is zero. Such result is primarily attributed to the broadband emittance feature of the dual-layer coating, which enables the dual-layer coating to emit more thermal energy. Meanwhile, slightly superior solar reflectance of the dual-layer coating (~ 0.96) guarantees less solar heating effect compared with the porous monolayer coating (with ~ 0.95 solar reflectance). (b) Comparison of the theoretical net cooling powers of the dual-layer coating and the PDRC coatings in Ref. S2 and Ref. S3 at varying $T_{coating}$. (c) The spectral reflectance of the ideal broadband coating, ideal selective coating and PDRC coatings in Ref. S2 and Ref. S3.

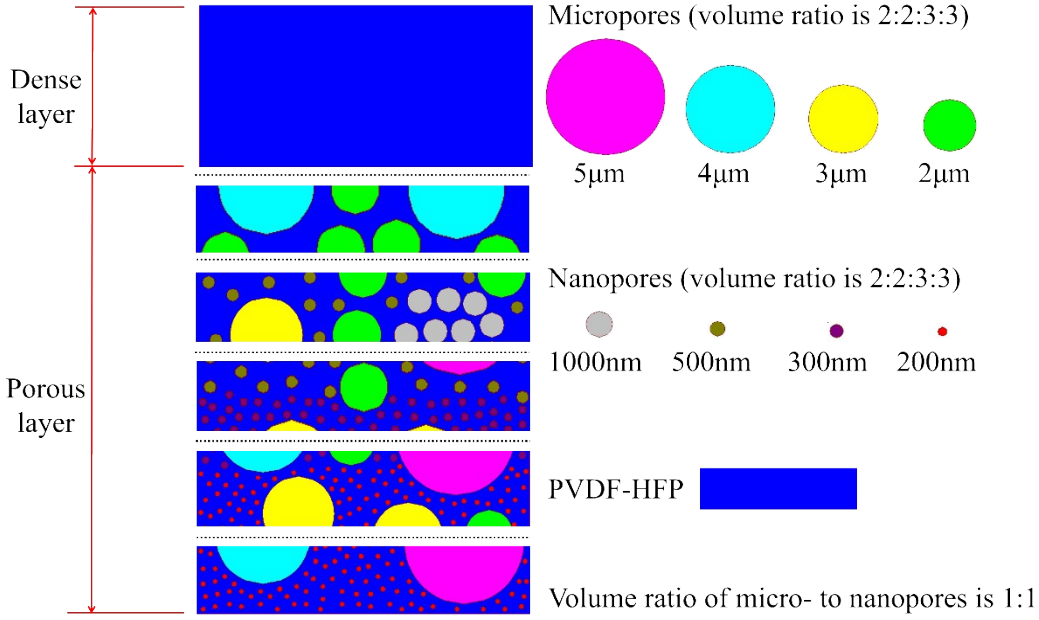

Fig. S10. The schematic illustration of the simulated structure of the dual-layer coating in the Rsoft.

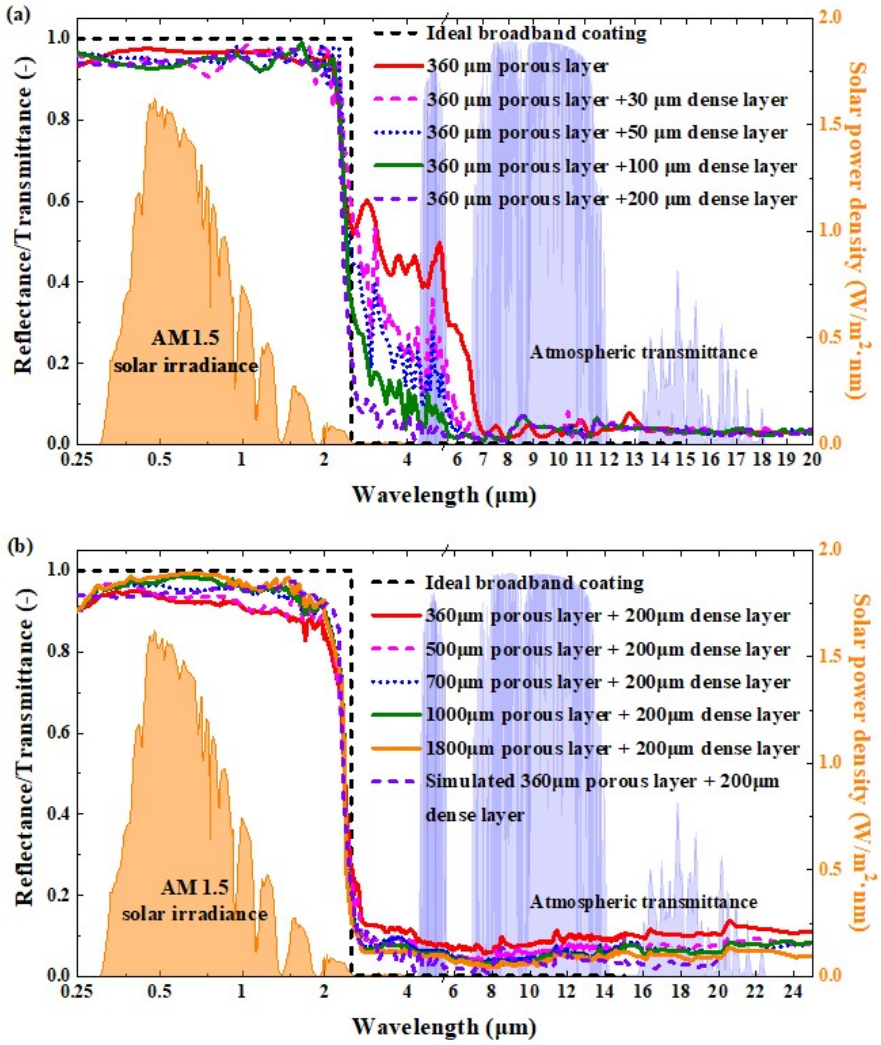

Fig. S11. The spectral reflectance of the dual-layer coating at varying thicknesses of the dense layer or porous layer. (a) The theoretically simulated spectral reflectance at varying thicknesses of the dense layer (b) the experimentally-characterized spectral reflectance at discrepant thicknesses of the porous layer. The dual-layer coatings with different thicknesses of the porous layers were prepared by varying the amount of the PVDF-HFP precursor colloid casted on the dense layer.

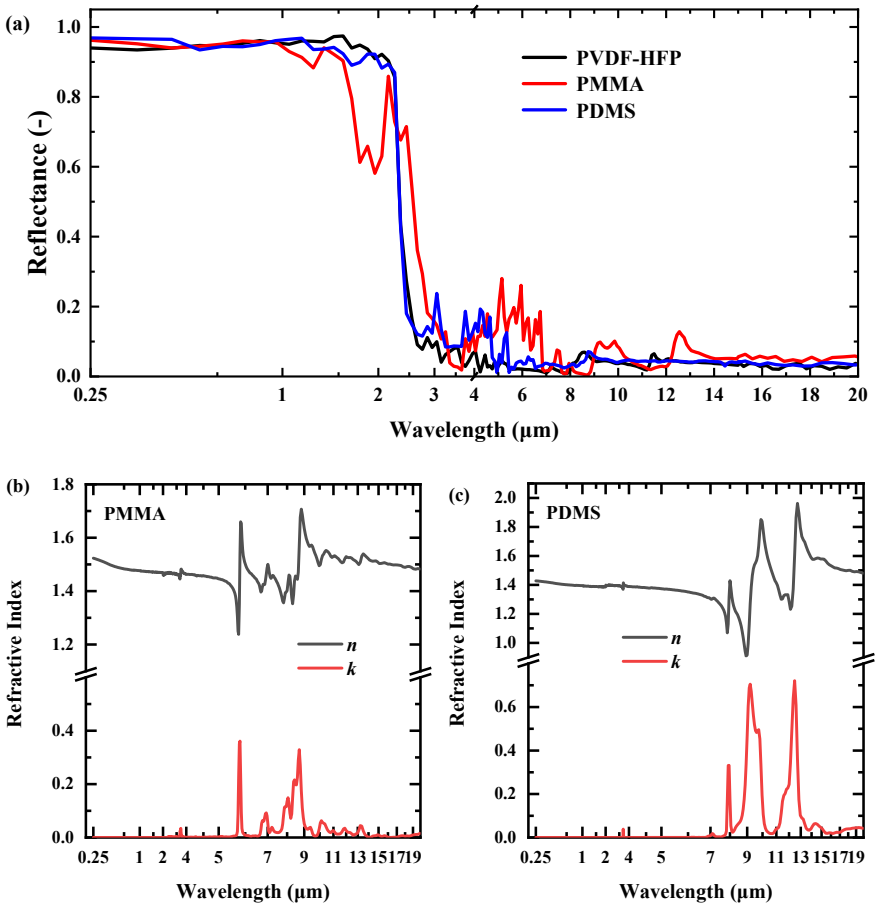

Fig. S12. Simulation of the spectral reflectance of the dual-layer coating composed of different polymer materials. (a) The simulated spectral reflectance of the dual-layer coatings with 200 μm-thick dense layer and 360 μm-thick porous layer, made of the poly(vinylidene fluoride-co-hexafluoropropene) (PVDF-HFP), polymethyl methacrylate (PMMA) and polydimethylsiloxane (PDMS), respectively. Though fluctuation occurs in the wavelength range of 3-8 μm, the reflectance of both PMMA and PDMS sharply reduces at the wavelength of ~2.5 μm, achieving a near-ideal broadband emission. (b and c) The complex refractive index of the PMMA (b) and PDMS (c), respectively.[10]

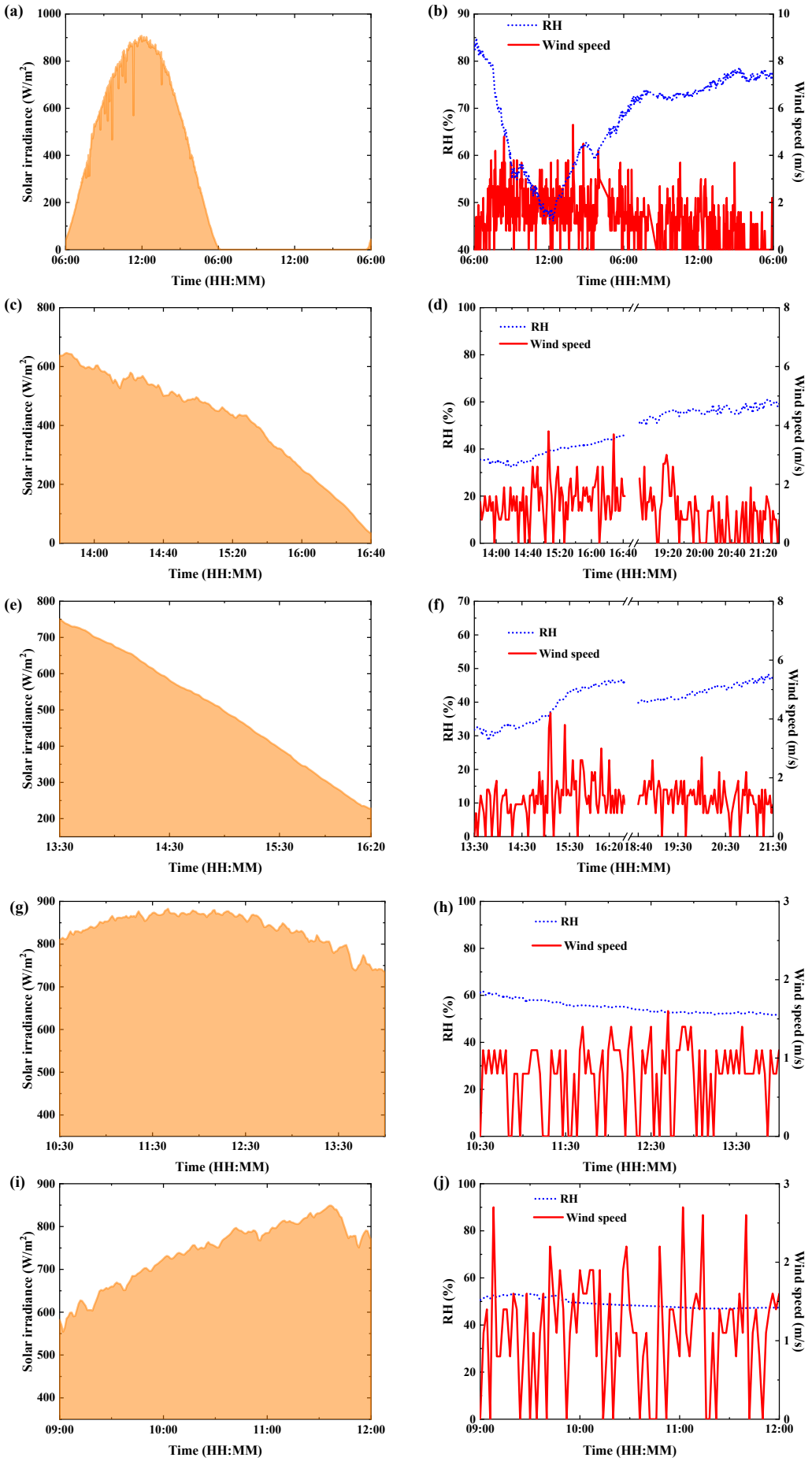
(a)
Solar irradiance (W/m²)
Time (HH:MM)
(b)
RH
Wind speed
RH (%)
Wind speed (m/s)
Time (HH:MM)
(c)
Solar irradiance (W/m²)
Time (HH:MM)
(d)
RH
Wind speed
RH (%)
Wind speed (m/s)
Time (HH:MM)
(e)
Solar irradiance (W/m²)
Time (HH:MM)
(f)
RH
Wind speed
RH (%)
Wind speed (m/s)
Time (HH:MM)
(g)
Solar irradiance (W/m²)
Time (HH:MM)
(h)
RH
Wind speed
RH (%)
Wind speed (m/s)
Time (HH:MM)
(i)
Solar irradiance (W/m²)
Time (HH:MM)
(j)
RH
Wind speed
RH (%)
Wind speed (m/s)
Time (HH:MM)

Fig. S13. The recorded solar irradiance, relative humidity (RH) and wind speed during the experimental periods: (a and b) in Fig. 4c and d (6 to 7 Sep., 2020); (c and d) in Fig. 4e and f (16 Dec., 2020); (e and f) in Fig. 5a and b (8 Nov., 2020); (g and h) in Fig. 5e and f (7 Sep., 2022); (i and j) in Fig. 5g and h (26 Sep., 2021).

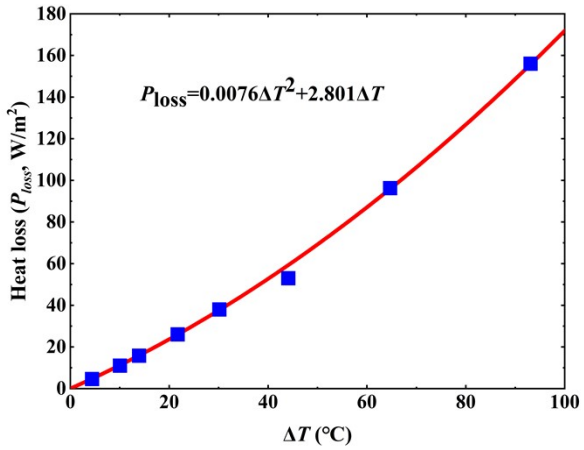

Fig. S14. The relation between the heat loss from the test chamber and the temperature difference ($\Delta T = T_{chamber} - T_a$; $T_{chamber}$, the temperature of the chamber without the PDRC coating) based on the experimental measurement. Notably, the P_{loss} becomes substantial with the increase of ΔT.

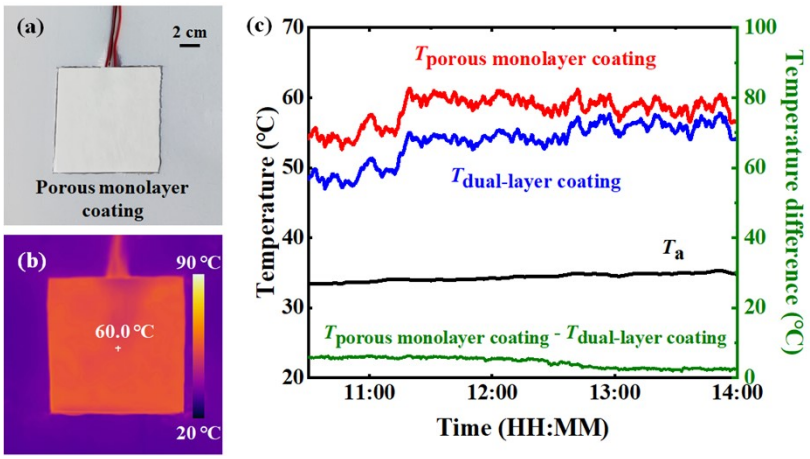

Fig. S15. (a and b) The photographic and infrared images of the copper plate covered with the porous monolayer coating. The size of the copper plate is 10 cm × 10 cm × 0.1 cm. (c) The temperature variation of the ambience (T_a), copper plate covered with dual-layer coating ($T_{dual\text{-}layer\ coating}$) and with porous monolayer coating ($T_{porous\ monolayer\ coating}$), along with the temperature difference between $T_{porous\ monolayer\ coating}$ and $T_{dual\text{-}layer\ coating}$ on 7 Sep., 2022.

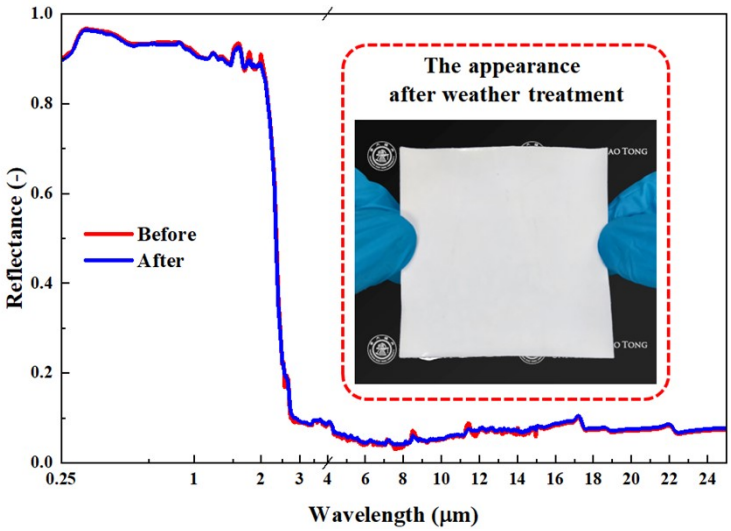

Fig. S16. The spectral reflectance of the dual-layer coating before and after being exposed outdoors for about 80 days. The inset is the appearance of the specimen after weather treatment. The dual-layer coating used in the weather treatment is composed of a 50 μm-thick dense layer and a 250 μm-thick porous layer.

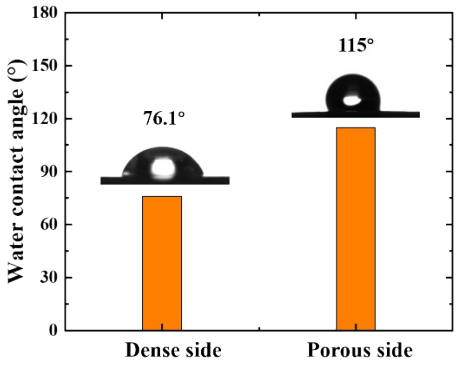

Fig. S17. The water contact angle on both sides of the dual-layer coating.

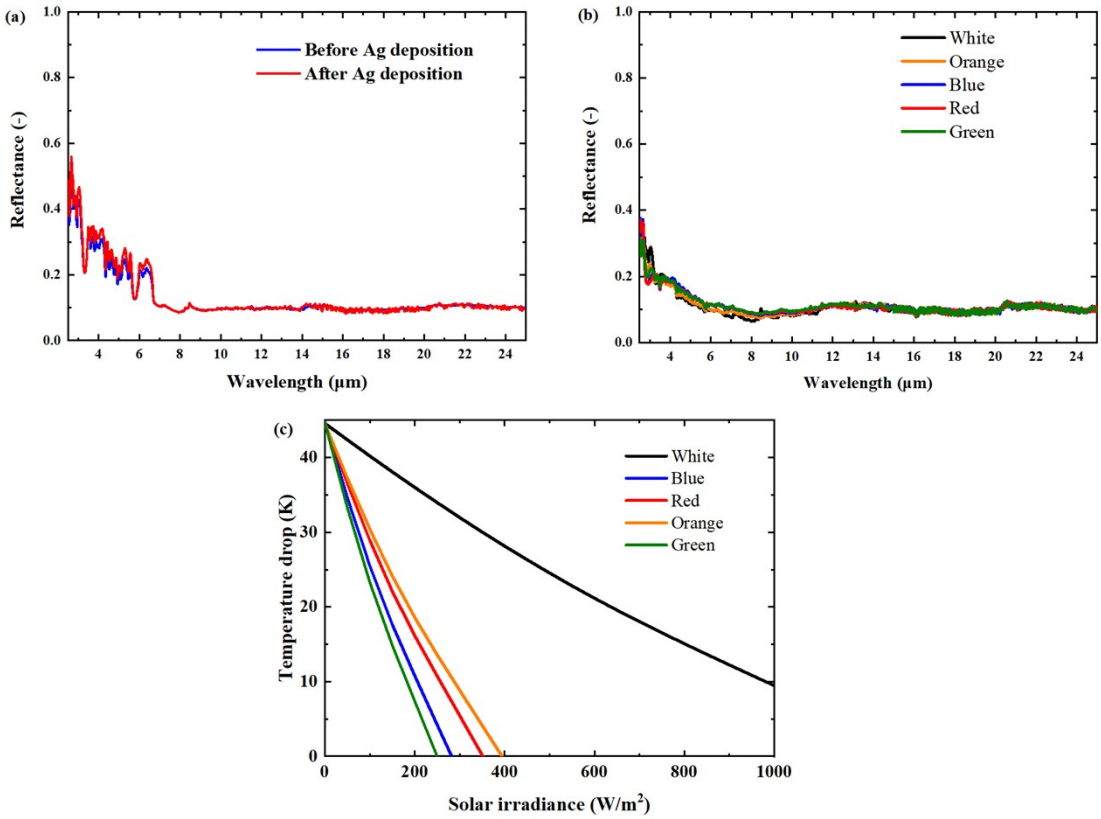

Fig. S18. The reflectance of the dual-layer coating over the wavelength range of 2.5-25 μm (a) Before and after the Ag deposition; (b) Before and after painted with four different colours; (c) The maximum temperature drops versus the solar irradiance of the dual-layer coatings before and after painted with four different colours. It can be seen that, with the increase of the incident solar irradiation, the maximum temperature drops of these colourful dual-layer coatings decrease rapidly, revealing that the sub-ambient radiative cooling effect of the colourful dual-layer coating is degraded due to the inevitable reflectance loss. And the values of the solar irradiance, as the maximum temperature drop is zero, are 394.24, 281.99, 351.60 and 249.60 W/m^2 for the orange, blue, red and green specimens, respectively.

Supplemental Video

Video S1. Large-scale production process of the dual-layer coating.

Supplemental References

1 J. Chen, L. Lu, Q. Gong, W. Y. Lau and K. H. Cheung, *Energy Conversion and Management*, 2021, **245**, 114621.

2 B. Xiang, R. Zhang, Y. Luo, S. Zhang, L. Xu, H. Min, S. Tang and X. Meng, *Nano Energy*, 2020, **81**, 105600.
3 H. Zhong, P. Zhang, Y. Li, X. Yang, Y. Zhao and Z. Wang, *ACS Applied Materials & Interfaces*, 2020, **12**, 51409-51417.
4 S.-Y. Heo, G. J. Lee, D. H. Kim, Y. J. Kim, S. Ishii, M. S. Kim, T. J. Seok, B. J. Lee, H. Lee and Y. M. Song, *Science Advances*, 2020, **6**, eabb1906.
5 M. Chen, D. Pang, J. Mandal, X. Chen, H. Yan, Y. He, N. Yu and Y. Yang, *Nano Letters*, 2021, **21**, 1412-1418.
6 D. Dendi, S. N. Ajong, G. Amori and L. Luiselli, *Diversity*, 2021 **13**, 388.
7 D. Xie, Z. Yang, X. Liu, S. Cui, H. Zhou and T. Fan, *Soft Matter*, 2019, **15**, 4294-4300.
8 J. Mandal, Y. Fu, A. C. Overvig, M. Jia, K. Sun, N. N. Shi, H. Zhou, X. Xiao, N. Yu and Y. Yang, *Science*, 2018, **362**, 315-318.
9 M. I. Mishchenko and P. Yang, *Journal of Quantitative Spectroscopy & Radiative Transfer*, 2018, **205**, 241-252.
10 X. Zhang, J. Qiu, J. Zhao, X. Li and L. Liu, *Journal of Quantitative Spectroscopy and Radiative Transfer*, 2020, **252**, 107063.